The Astrophysical Journal Letters, 861:L3 (8pp), 2018 July 1 https://doi.org/10.3847/2041-8213/aacce6

Keck/Palomar Cosmic Web Imagers Reveal an Enormous Lyα Nebula in an Extremely Overdense Quasi-stellar Object Pair Field at $z = 2.45$

Zheng Cai[1,6], Erika Hamden[2], Matt Matuszewski[2], J. Xavier Prochaska[1], Qiong Li[3], Sebastiano Cantalupo[4], Fabrizio Arrigoni Battaia[5], Christopher Martin[2], James D. Neill[2], Donal O'Sullivan[2], Ran Wang[3], Anna Moore[2], and Patrick Morrissey[2]
[1] UCO/Lick Observatory, University of California, 1156 High Street, Santa Cruz, CA 95064, USA
[2] Cahill Center for Astrophysics, California Institute of Technology, 1216 East California Boulevard, Mail code 278-17, Pasadena, CA 91125, USA
[3] Kavli Institute for Astronomy and Astrophysics, Peking University, Beijing 100871, People's Republic of China
[4] Department of Physics, ETH Zurich, CH-8093, Zurich, Switzerland
[5] European Southern Observatory, Karl-Schwarzschild-Str. 2, D-85748 Garching bei Marcsecunchen, Germany
Received 2018 March 26; revised 2018 May 28; accepted 2018 June 12; published 2018 June 26

Abstract

Enormous Lyα nebulae (ELANe) represent the extrema of Lyα nebulosities. They have detected extents of >200 kpc in Lyα and Lyα luminosities $>10^{44}$ erg s^{-1}. The ELAN population is an ideal laboratory to study the interactions between galaxies and the intergalactic/circumgalactic medium (IGM/CGM) given their brightness and sizes. The current sample size of ELANe is still very small, and the few $z \approx 2$ ELANe discovered to date are all associated with local overdensities of active galactic nuclei (AGNs). Inspired by these results, we have initiated a survey of ELANe associated with quasi-stellar object (QSO) pairs using the Palomar and Keck Cosmic Web Imagers (PCWI/KCWI). In this Letter, we present our first result: the discovery of ELAN0101+0201 associated with a QSO pair at $z = 2.45$. Our PCWI discovery data shows that, above a 2σ surface brightness of 1.2×10^{-17} erg s^{-1} cm^{-2} arcsec^{-2}, the end-to-end size of ELAN0101+0201 is $\gtrsim$232 kpc. We have conducted follow-up observations using KCWI, resolving multiple Lyα emitting sources within the rectangular field of view of $\approx 130 \times 165$ projected kpc^2, and obtaining their emission line profiles at high signal-to-noise ratios (S/Ns). Combining both KCWI and PCWI, our observations confirm that ELAN0101+0201 resides in an extremely overdense environment. Our observations further support that a large amount of cool ($T \sim 10^4$ K) gas could exist in massive halos ($M \gtrsim 10^{13}\, M_\odot$) at $z \approx 2$. Future observations on a larger sample of similar systems will provide statistics of how cool gas is distributed in massive overdensities at high redshift and strongly constrain the evolution of the intracluster medium.

Key words: galaxies: halos – galaxies: high-redshift – intergalactic medium – quasars: emission lines

1. Introduction

Recent observations have lead to the discovery of the first sample of enormous Lyα nebulae (ELANe) at $z = 2$–3 (Cantalupo et al. 2014; Hennawi et al. 2015; Cai et al. 2017; Arrigoni Battaia et al. 2018). ELANe are defined as nebulae with Lyα sizes greater than 200 kpc and Lyα luminosities greater than 10^{44} erg s^{-1}. Their Lyα sizes exceed the diameter of a $10^{12.5}\, M_\odot$ halo, typical mass of quasi-stellar object (QSO) host halos (White et al. 2012). Their morphology and kinematics are ideal properties to constrain models of galaxy formation, galaxy-intergalactic medium (IGM) interactions, and galaxy interactions that possibly happen in the highest overdense regions (Martin et al. 2015; Arrigoni Battaia et al. 2018).

Although Lyα nebulae with sizes of 100 kpc are commonly found around luminous QSOs at $z \gtrsim 3$ (Borisova et al. 2016), only two out of 17 nebulae in this sample have sizes >200 kpc, which meet the ELANe definition. At $z \approx 2$, QSO-Lyα nebulae appear to be rarer. Arrigoni Battaia et al. (2016) conducted deep narrowband images on 15 $z \approx 2.2$ QSOs and did not detect bright nebulae with SB $\approx 10^{-17}$ erg s^{-1} cm^{-2} arcsec^{-2} at distances >50 kpc around any of these QSOs.

All $z \approx 2$ ELANe found to date reside in local active galactic nucleus (AGN) overdensities: the Slug and MAMMOTH-1 nebulae (Cantalupo et al. 2014; Cai et al. 2017) contain two AGNs. The Jackpot nebula (Hennawi et al. 2015) is associated with an AGN quartet. Photoionization is often involved in interpreting these large nebulosities. There are two possible reasons for these detections. A stronger UV radiation field may boost the extended Lyα emission into the detectable regime (Cantalupo et al. 2005; Kollmeier et al. 2010), and a higher circumgalactic medium (CGM) density may also yield brighter Lyα fluorescence (e.g., Cantalupo et al. 2012). Thus, AGN pairs or groups may be ideal sites to search for ELANe, because they provide both the strong meta-galactic ionizing fluxes and gas overdensities required for detections. This has motivated our survey using QSO pairs. In addition, recent studies have suggested that Sloan Digital Sky Survey (SDSS) QSO pairs trace protoclusters (Onoue et al. 2018), and thus the extended Lyα, C IV, He II lines traced by QSO pairs can be used to probe cool ($T \sim 10^4$ K) and warm ($T \sim 10^5$ K) gas in the early intracluster medium (ICM; Valentino et al. 2016).

Guided by the above observational and theoretical insights, we have conducted a survey using the Palomar and Keck Cosmic Web Imagers (PCWI/KCWI) to search for ELANe associated with QSO pairs at $z \approx 2$. Our goals are to significantly enlarge the number of confirmed ELANe at $z \approx 2$, and then systematically understand the gas budget and kinematics throughout the dark matter halos of these objects. Our results will be compared to nebulae powered by isolated

[6] Hubble Fellow.

QSOs at $z \approx 2$–3 and further used to constrain the ICM evolution.

In this Letter, we present our first discovery in the survey: ELAN0101+0201, associated with the QSO pair at $z = 2.4$ using both PCWI and KCWI observations. The projected separation of these two QSOs is $\approx 10''$ (82.5 physical projected kpc) and the redshift separation is about $1000\,\mathrm{km\,s^{-1}}$. The brighter QSO (Q1) has an AB magnitude of $i = 18.1$ and the fainter QSO (Q2) has $i = 21.6$ ($\approx$30 times fainter than Q1). The statistical results on the full sample of 12 sources will be presented in upcoming papers. In Section 2, we introduce our observations and data reductions. In Section 3, we provide the discovery of the ELAN and the gas kinematics. In Section 4, we provide a discussion of the results. We assume a ΛCDM cosmology with $\Omega_m = 0.3$, $\Omega_\Lambda = 0.7$, and $h = 0.70$.

2. Observations

2.1. Sample Selection

We searched for QSO pairs from the SDSS-IV QSO database, which contains ~200,000 QSO spectra at $2.0 < z < 2.5$ (Pâris et al. 2017). Our sample contains 12 QSO pairs, where each consists of two QSOs with 2D separation smaller than 1′, and velocity offset $<2000\,\mathrm{km\,s^{-1}}$. Further, we require at least one of them to have $g < 19$. The observations are conducted in two stages. Stage 1 is a shallow PCWI program to search for extended emission; stage 2 is a deeper targeted search with KCWI to conduct high-resolution, high signal-to-noise observations to study the gas kinematics and emission lines in greater detail. ELAN0101+0201, at $z \approx 2.4$, is our first target from this sample with both PCWI and follow-up KCWI data. The systemic redshift of Q1 is at $z = 2.4521 \pm 0.0004$, fitted from the Mg II emission. The Lya redshift of Q1 is at $z = 2.4510 \pm 0.0002$. Q2 does not have sufficient S/N around Mg II to determine the systemic redshift, and it has a Lyα redshift of 2.4513 ± 0.0003. Q1 and Q2 have a consistent Lyα redshift.

2.2. PCWI and KCWI Observations, Data Reduction

The PCWI observations of ELAN0101+0201 were carried out on UT-20161130 and UT-20171215. The total exposure time is 4 hr on-source and 4 hr on the blank sky. Individual exposures were acquired using the standard CWI nod-and-shuffle technique (Martin et al. 2014). PCWI uses a $40'' \times 60''$ reflective image slicer with 24 $40'' \times 2\farcs5$ slices. We put the brighter QSO (Q1) at the integral field unit (IFU) center. We used the Richardson grating ($R = 2000$) and an Asahi/blue filter. We use the standard CWI pipeline to reduce the data (Martin et al. 2014).

The KCWI observations of ELAN0101+0201 were carried out on UT-20171021 and UT-20171119. The BM1 grating and medium slicer were chosen. This setting yields a field of view (FoV) of $16\farcs8 \times 20''$, and a spatial resolution of $\approx 0\farcs7$ along the slicer and seeing-limited sampling ($\approx 1\farcs0$) perpendicular to the slicer. The spectral resolution is $R = 4000$. The datacube has wavelength coverage of $\lambda = 3950$–4800 Å, centered on the QSO-Lyα redshift ($\lambda \approx 4200$ Å). The total on-source exposure time is 120 minutes, in four 10-minute and four 20-minute individual exposures. To maximize the observing efficiency, we used the "offset-target-field" to construct the sky datacube, rather than nod-and-shuffle. The offset target has a different redshift and is within two degrees of ELAN0101+0201. We obtained the sky of each wavelength channel using the median value after masking the point source of the offset target. The KCWI pipeline[7] was used to reduce the data. For each image, we subtracted the bias, corrected the pixel-to-pixel variation, removed cosmic rays, corrected the geometric transformation, and performed the wavelength calibration. For each channel, we subtracted the sky determined by the offset-target field. Flux calibration was performed using the standard star BD+28D4211 at the beginning of the night. The final datacube is combined from the inverse variance weight of individual exposures. In addition, we used the CubeExtractor package to further perform the high-order flat-field corrections and to remove the point-spread function (PSF) of the bright QSO (Q1; S. Cantalupo 2018, in preparation; see also Borisova et al. (2016) for a description of main routines).

3. Results

3.1. The Discovery of an Enormous Lyα Nebula

In the upper-left panel of Figure 1, we present the PCWI PSF-subtracted Lyα narrowband image. The 4 hr on-source integration with nod-and-shuffle mode yields a $1\sigma_{\rm SB}$ of $4.5 \times 10^{-18}\,\mathrm{erg\,s^{-1}\,cm^{-2}\,arcsec^{-2}}$ over a velocity range of $\pm 500\,\mathrm{km\,s^{-1}}$ around the systemic redshift of Q1 ($z = 2.4510 \pm 0.0003$). To a $2\sigma_{\rm SB}$ contour, the ELAN has an extended size of $27\farcs9$, corresponding to a physical size of 232.2 kpc. The total Lyα luminosity of ELAN0101+0201 is $L_{\rm Ly\alpha} = 4.5 \times 10^{44}\,\mathrm{erg\,s^{-1}}$.

In the upper-right panel of Figure 1, we present the KCWI observations. The size of the ELAN exceeds the KCWI FoV (orange box). The 2 hr integration yields a flux density of $1\sigma \approx 2.4 \times 10^{-19}\,\mathrm{erg\,s^{-1}\,cm^{-2}\,Å^{-1}}$, corresponding to a $1\sigma_{\rm SB}$ of $1.0 \times 10^{-18}\,\mathrm{erg\,s^{-1}\,cm^{-2}\,arcsec^{-2}}$ over a velocity range of $\pm 500\,\mathrm{km\,s^{-1}}$ around the systemic redshift of Q1, a factor of $\approx 5\times$ deeper than PCWI observations. KCWI has a much higher spatial resolution for resolving the sub-structures in the Lyα nebula. Both PCWI and KCWI detect extended Lyα emission and a projected filament that appears to connect both QSOs (yellow asterisks in Figure 1). From Section 2.1, Q1 and Q2 have a consistent Lyα redshift. We do not observe a statistically significant velocity offset from the position of Q1 to the position of Q2 (Figures 1 and 2). A higher spectral resolution may be able to distinguish the velocity gradient between Q1 and Q2.

3.2. The Kinematics of the Lyα Nebula

From the KCWI observations, we derive a flux-weighted velocity map (Figure 1, lower left). The zeropoint of the velocity is set at the systemic redshift of Q1 ($z = 2.4510$), determined from the Mg II emission in the SDSS spectrum. From the velocity map, there are no clear velocity structures (e.g., rotation or bipolar outflow signatures). The majority of the nebula has a velocity offset within $\pm 150\,\mathrm{km\,s^{-1}}$ from the zeropoint. A high-velocity component with $v \gtrsim 150\,\mathrm{km\,s^{-1}}$ is seen in the northwest, and this component corresponds to a LAE discussed below. The velocity dispersion map (Figure 1, bottom right) is obtained using the second moment of the flux distribution. The majority of the nebula has a velocity dispersion $\lesssim 250\,\mathrm{km\,s^{-1}}$, indicating a Lyα line width of

[7] KCWI pipeline: https://github.com/kcwidev/kderp.

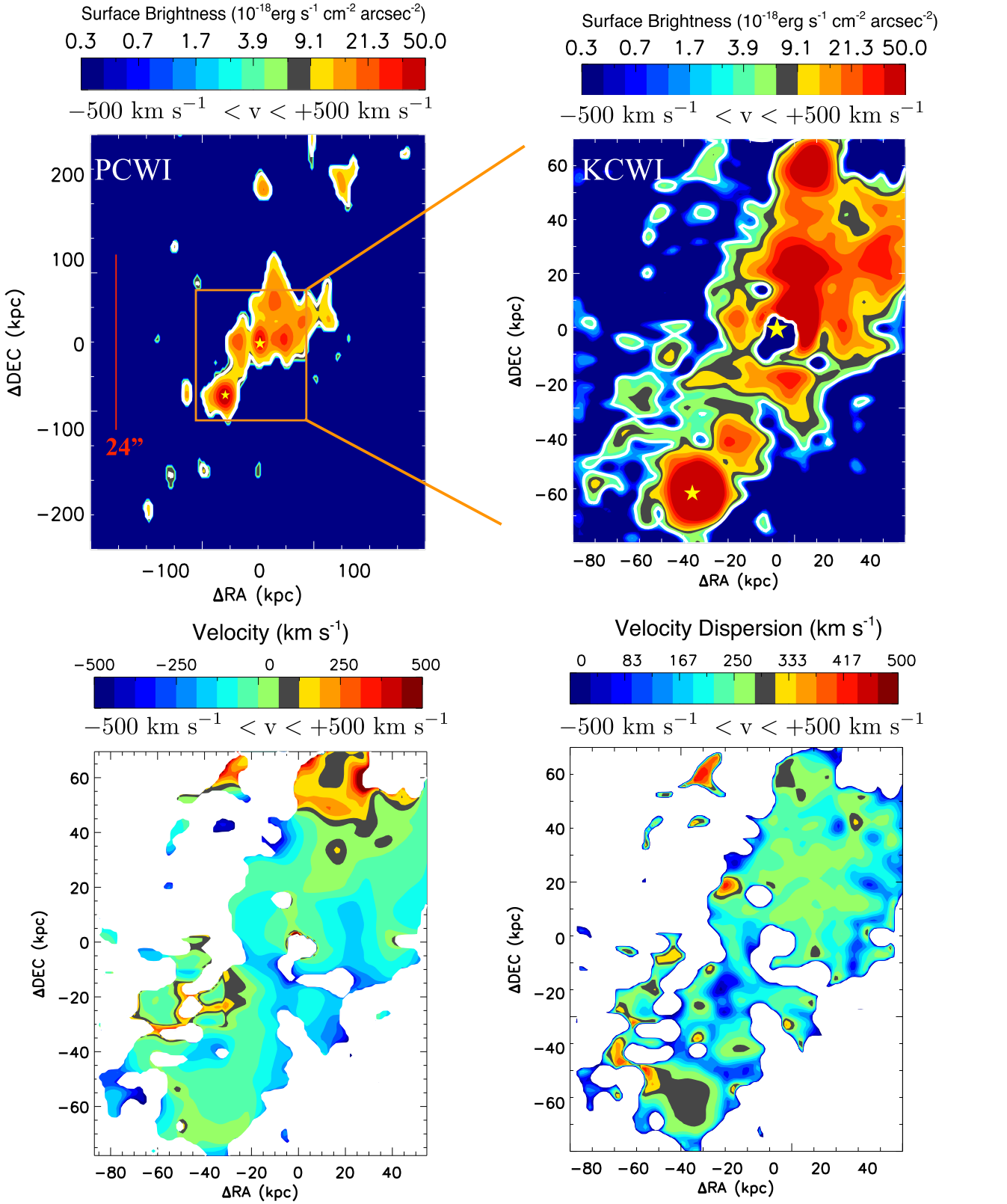

Figure 1. The upper-left panel shows the PSF-subtracted narrowband image of the ELAN0101+0201 observed using the PCWI. From PCWI observations, this Lyα nebula has an end-to-end size of 232 kpc. With 8 hr PCWI nod-and-shuffle observations, the 1σ surface brightness (SB) limit is 4.5 $\times$ 10^{-18} erg s^{-1} cm^{-2} arcsec^{-2}. The white contour presents the 2σ SB level. The upper-right panel shows the PSF-subtracted KCWI high-resolution Lyα image. The KCWI FoV is marked by the orange box in the left panel. The 1σ SB limit is $\approx$1 $\times$ 10^{-18} erg s^{-1} cm^{-2} arcsec^{-2} (the white curve indicates the 3σ SB contour). The lower two panels show the flux-weighted velocity and the flux-weighted velocity dispersion map using KCWI. Note that the PCWI and KCWI narrowband images have some differences, especially around Q1; this is because of the PSF subtraction. The PCWI PSF is very different than that of KCWI, because the two IFU data have many different properties, including the very different seeing conditions, optical settings, and spatial/spectral resolutions.

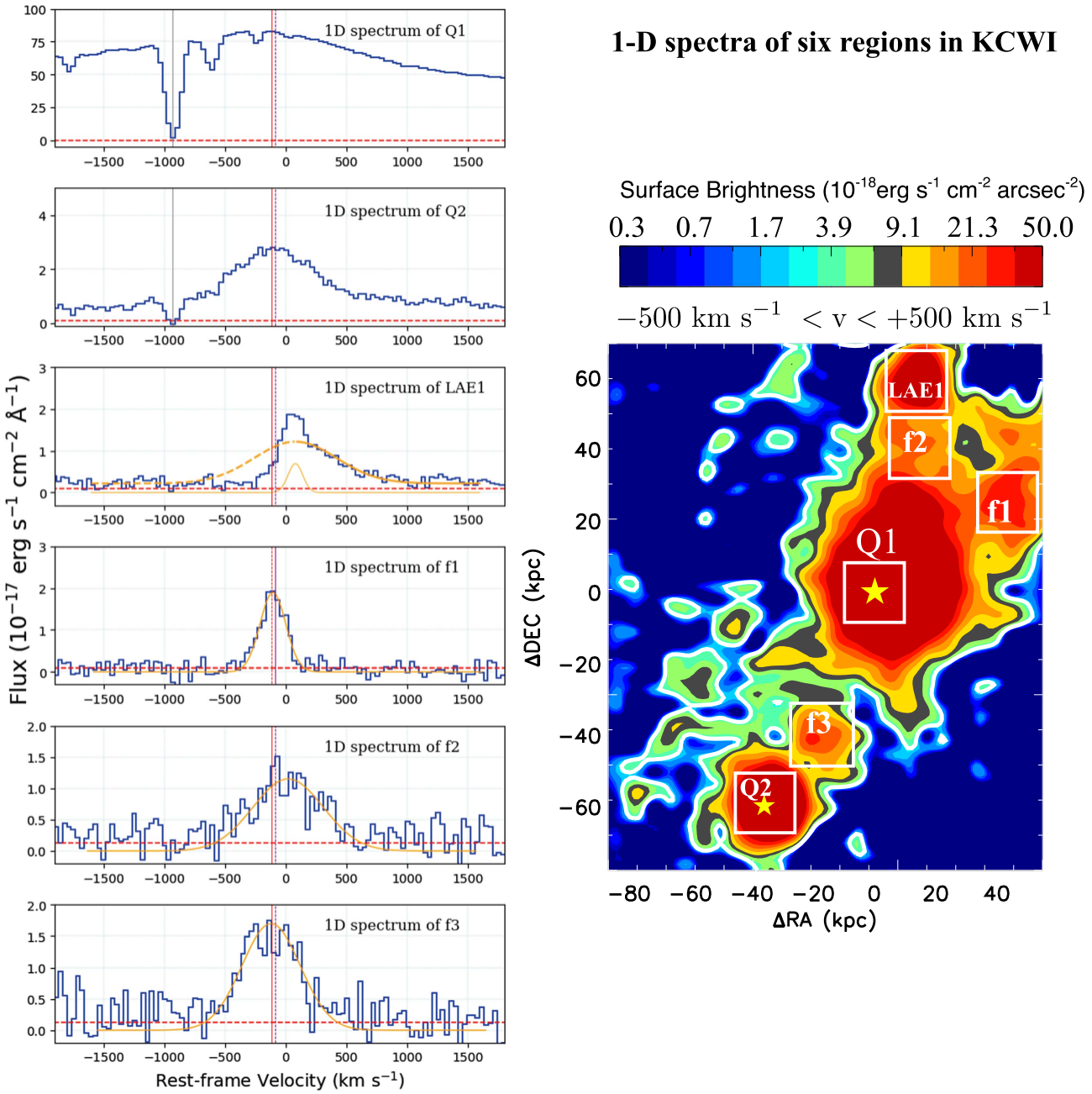

Figure 2. 1D spectra (blue line) extracted from the KCWI datacube with the noise overplotted (red dotted line). The zeropoint is set using the systemic redshift of Q1. The vertical red indicates the Lyα redshift of Q1, and the vertical dashed purple indicates the Lyα redshift of Q2. We extract six regions: brighter QSO (Q1), fainter QSO (Q2), one Lyα emitter (LAE1), and three brighter nodes in the nebular region (f1, f2, and f3). We mark strong Lyα absorption detected in the spectra of Q1 and Q2 using gray vertical lines. For the Lyα emission of LAE1, we use one broad (thick orange line) with the FWHM of 840 km s^{-1} and one narrow component (thin orange line) with the FWHM of 170 km s^{-1}. The blue wing of the broad component is significantly absorbed (dotted yellow line). The Lyα emission of f1, f2, and f3 can be fit with a single Gaussian. Note that the KCWI narrowband image in Figure 2 is different from Figure 1. This is because in Figure 2, we do not subtract the Q1 PSF in order to show the absorption system in the spectrum of the QSO continuum.

$\lesssim$587 km s^{-1} throughout most of the nebular region covered by KCWI.

3.3. Overdensity of Lyα Emitters

In Figure 2, we show six 1D spectra from the KCWI datacube, including Q1, Q2, and a KCWI resolved bright LAE (LAE1). The positions labeled f1, f2, and f3 are bright nodes in the nebular region resolved by KCWI.

LAE1 has a higher velocity than the nebular redshift (Figure 1). Figure 2 shows that LAE1 has a highly asymmetric Lyα profile. The Lyα emission can be fit using one broad (thick orange line) component with the FWHM of 840 km s^{-1} and one narrow component (thin orange line) with the FWHM of 170 km s^{-1}. The left wing of the broad component is strongly absorbed. The possible causes of this absorption are discussed in Section 4.3. f1 and f3 have the Lyα redshift consistent with that of the QSO pair system. f2 has 80 km s^{-1}

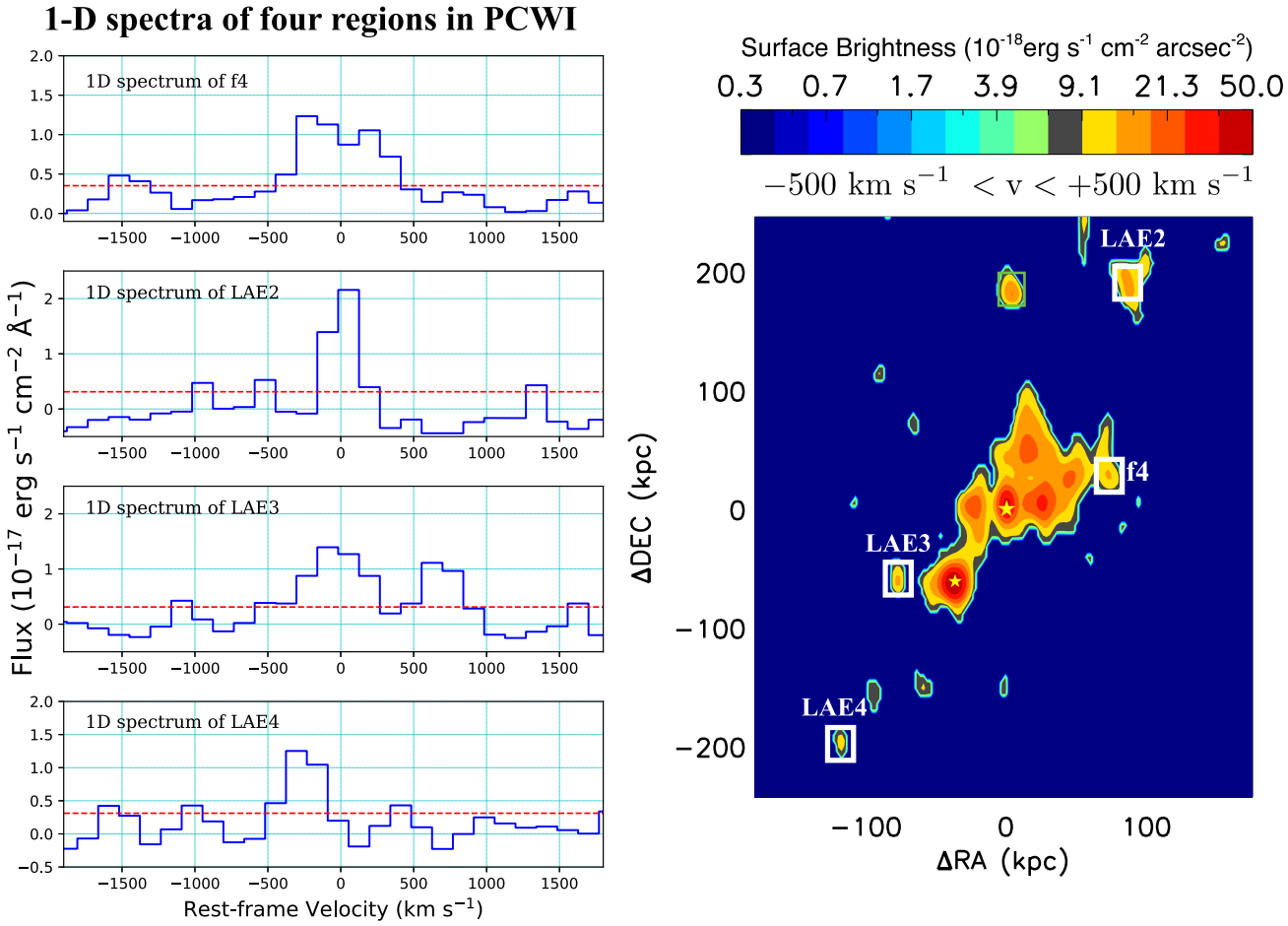

Figure 3. 1D spectra (blue line) extracted from the PCWI datacube with the noise overplotted (red). We extract four sources outside of the KCWI field of view (white rectangles). LAE2, LAE3, and LAE4 are three LAE candidates with the emission lines >5σ over 2″ × 3″ apertures. We extract the 1D spectrum of a nebular region (f4). Including LAE1 resolved by KCWI (Figure 2), we demonstrate that ELAN0101+0201 is embedded in a significantly overdense field (see details in Section 4.2). There is a bright source in the PCWI, marked by a green rectangle, that is a [O II] interloper at $z = 0.12$.

Table 1
Sources in the Field of ELAN0101+0201

Name	R.A.	Decl.	z	$L_{\mathrm{Ly}\alpha}$ (10^{42} erg s^{-1})	Integral Field Spectroscopy (IFS)
Q1 (brighter QSO)	01:01:16.54	+02:01:57.4	2.4521 (Mg II)	802.0	KCWI
Q2 (fainter QSO)	01:01:16.85	+02:01:49.8	2.4513 (Lyα)	10.1	KCWI
LAE1 (could be an AGN)	01:01:16.44	+02:02:04.5	2.462 (Lyα)	2.90 ± 0.03	KCWI
LAE2	01:01:16.30	+02:02:25.2	2.449 (Lyα)	2.8 ± 0.2	PCWI
LAE3	01:01:16.45	+02:01:50.0	2.453 (Lyα)	3.1 ± 0.2	PCWI
LAE4	01:01:17.34	+02:01:38.5	2.446 (Lyα)	1.6 ± 0.2	PCWI

higher velocity than the QSO pair system, bridging Q1 and LAE1.

In Figure 3, we show four 1D spectra from the PCWI datacube using a 2″ × 3″ aperture. All of the sources have >5σ detection of the emission lines. These sources reside outside of the KCWI FoV. Assuming that all of these emission lines are Lyα, their Lyα luminosities are $L_{\mathrm{Ly}\alpha} = (1.6\text{–}3.2) \times 10^{42}$ erg s^{-1} ($L^{*}_{\mathrm{Ly}\alpha} = 2.1 \times 10^{42}$ erg s^{-1}; Ciardullo et al. 2012). Including LAE1, we detect four LAE candidates and two QSOs in an 40″ × 60″ area, within a redshift range of $z = 2.44\text{–}2.46$ (Table 1).

3.4. The Pair of Lyα Absorbers

In the spectra of Q1 and Q2, we detect strong Lyα absorbers at −710 km s^{-1} in reference to QSO-Lyα emission ($z = 2.441$; gray vertical lines in Figure 2). Using a Markov-Chain Monte Carlo (MCMC) analysis (Figure 4), we found that the column density of both absorbers have $N_{\mathrm{H\,I}} \approx 10^{15-18}$ cm^{-2} in >95.5% (Figure 4). These absorbers are not associated with any Lyα-emitting galaxies in the KCWI observed field within a velocity offset of ±1000 km s^{-1} around the absorption redshift. Within the KCWI FoV, we put a 5σ upper limit of 0.1 $L^{*}_{\mathrm{Ly}\alpha}$ for the counterpart galaxy within $R \approx 50$ projected kpc around Q1.

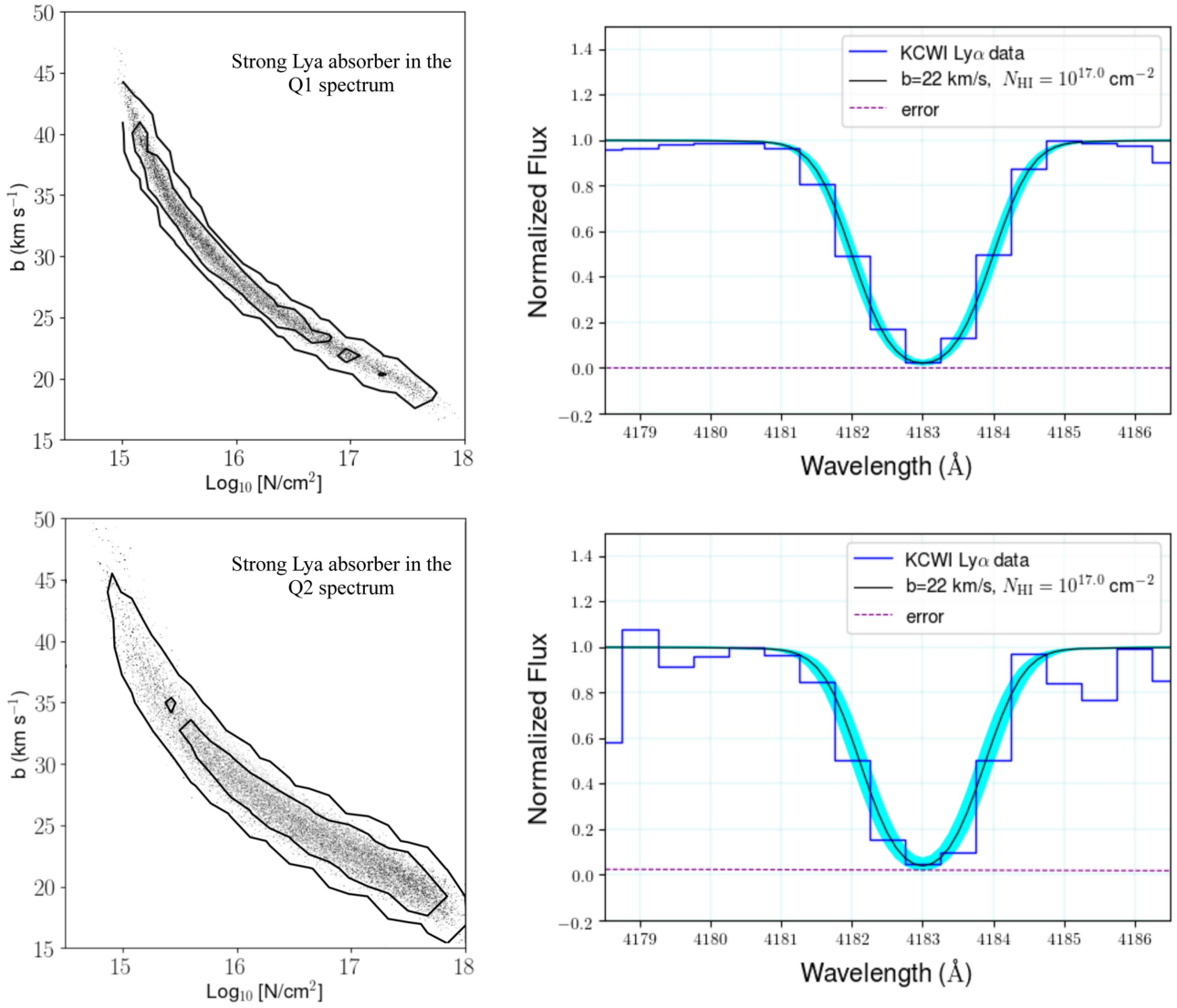

Figure 4. MCMC analysis of the column density ($N_{\rm H\,I}$) and Doppler parameter (b) of the strong absorbers in the spectrum of Q1 (upper) and Q2 (lower). The absorption system is marked by vertical gray lines in Figure 2. In the right panel, we provide the 1D absorber fit using $N_{\rm H\,I} = 10^{17}$ cm^{-2} and $b = 22$ km s^{-1}, with 1σ uncertainty using a cyan region. We did not detect galaxy counterparts associated with this absorption group from current data (see details in Section 3.4 and the Appendix).

This corresponds to a Lyα-based star formation rate (SFR) of $\lesssim$0.3 $M_\odot$ yr^{-1} (Kennicutt & Evans 2012). Within the PCWI FoV, we put a 5σ upper limit of $L_{\rm Ly\alpha} = 0.6\,L^*_{\rm Ly\alpha}$ within $R \lesssim 150$ projected kpc, corresponding to a Lyα-based SFR of $\lesssim$1.5 $M_\odot$ yr^{-1} (see more discussions in the Appendix).

4. Discussion

We have identified ELAN0101+0201 with an end-to-end size of $\gtrsim$232 kpc. Such a large and luminous nebula is rarely found, especially around $z \approx 2$ QSOs. The filament is elongated along the projected line connecting the two QSOs. With KCWI observations, we further resolved a LAE (LAE1 in Figure 2), which has a highly asymmetric Lyα emission.

4.1. The Enormous Nebula at z ≈ 2 and its Powering Mechanism

ELAN0101+0201 is associated with a $z \approx 2$ QSO pair. To understand the physical properties, we investigate the powering mechanism of this nebula. A few processes can power the extended Lyα emission: photoionization, shock-heated gas by an AGN outflow, and resonant scattering from the QSO broadline-region (Cantalupo 2017 for a review).

The kinematics analysis disfavors a strong outflow playing a major role in powering this nebula. The velocity map of ELAN0101+0201 (Figure 1) does not show obvious bipolar outflow signatures (Cai et al. 2017). Alexander et al. (2010) and Harrison et al. (2014) also suggested that AGN outflows have a high velocity of $v_{\rm max} \gtrsim 1500$ km s^{-1}, which is not the case for ELAN0101+0201. The velocity pattern is similar to nebulae found by Borisova et al. (2016) at $z \approx 3$. The velocity dispersion measurement (Section 3.2 and Figure 1) is consistent with a nebula illuminated by a radio-quiet system (FWHM < 700 km s^{-1}; Villar-Martín et al. 2007; Borisova et al. 2016).

We now consider the photoionization scenario. As Q2 is expected to be 30× fainter than Q1 and most nebular emission resides in the northwest region with respect to Q1 position, we assume that the nebula is photoionized by Q1. We consider both optically thin and thick CGM photoionized by Q1.

Following Hennawi & Prochaska (2013), the surface brightness of an optically thin cloud due to recombination can be expressed as follows:

$$SB_{\rm Ly\alpha}^{\rm thin} = 8.8 \times 10^{-20}\left(\frac{1+z}{3.253}\right)^{-4} \times \left(\frac{f_{\rm C}^{\rm thin}}{0.5}\right)\left(\frac{N_{\rm H}}{10^{20.5}\ {\rm cm^{-2}}}\right) {\rm erg\ s^{-1}\ cm^{-2}\ arcsec^{-2}}. \quad (1)$$

Arrigoni Battaia et al. (2015a, 2015b) and Hennawi et al. (2015) posited that the smooth Lyα morphology suggests the covering factor $f_{\rm C}^{\rm thin} \geqslant 0.5$. Here we assume that $f_{\rm C}^{\rm thin} = 0.5$. Using a statistical sample, Lau et al. (2016) found that $N_{\rm H} \approx 10^{20.5\pm1.0}\,{\rm cm^{-2}}$ within 200 kpc in the QSO halo. We thus assume $N_{\rm H} = 10^{20.5}\,{\rm cm^{-2}}$ in Equation (1). Given the average ${\rm SB_{Ly\alpha}} \approx 1 \times 10^{-17}\,{\rm erg\,s^{-1}\,cm^{-2}\ arcsec^{-2}}$ at $R \approx 50$ kpc from Q1, the hydrogen number density is $n_{\rm H} \approx 1\,{\rm cm^{-3}}$. This value is typical for the ISM, but it is not typical for CGM where simulations predict $n_{\rm H} \sim 10^{-3}\,{\rm cm^{-3}}$ (e.g., Shen et al. 2013). The ELAN0101+0201 has a CGM density 2–3 orders of magnitude higher than the statistical QSO sample at $z \sim 2$ (Arrigoni Battaia et al. 2016), suggesting that this QSO pair may contain an unusually high-density CGM compared to typical isolated QSOs at $z \sim 2$. Note that the optically thin scenario is also favored by previously discovered ELANe, such as the Slug and Jackpot nebulae. MAMMOTH-1 nebula (Cai et al. 2017) has Lyα FWHM of $2000\,{\rm km\,s^{-1}}$ over 30 kpc, much higher than that of other ELANe. This wide FWHM suggests that other than photoionization, MAMMOTH-1 ELAN may also be partially powered by AGN outflow.

If we consider the optically thick scenario, Hennawi & Prochaska (2013) suggested that the SB can be estimated as follows:

$$SB_{\rm Ly\alpha}^{\rm thick} = 5.3 \times 10^{-17}\left(\frac{1+z}{3.45}\right)^{-4}\left(\frac{f_{\rm C}^{\rm thick}}{0.5}\right)\left(\frac{R}{160\ {\rm kpc}}\right) \times \left(\frac{L_{\nu_{\rm LL}}}{10^{30.9}\ {\rm erg\,s^{-1}\,Hz^{-1}}}\right){\rm erg\,s^{-1}\,cm^{-2}\,arcsec^{-2}} \quad (2)$$

The i-band magnitude of the bright QSO is 18.1, and the inferred Log $\frac{L_{\nu_{\rm LL}}}{\rm erg\ s^{-1}} = 31.1$, obtained from scaling the composite QSO spectrum to match the i-band magnitude of Q1 (Arrigoni Battaia et al. 2015b; Lusso et al. 2015). Assuming that $f_{\rm C}^{\rm thick} = 0.5$, the predicted ${\rm SB_{Ly\alpha}} \sim 10^{-15}\,{\rm erg\,s^{-1}\,cm^{-2}}$ at $\approx$50 kpc from Q1, two orders of magnitude higher than the observed SB. Thus, the UV-illuminated optically thick gas may have a small covering factor, or the illumination due to optically thick gas is not the dominant powering mechanism.

4.2. The Association of Cool Gas and Overdense Environments at $z \approx 2$

Using the Hyper-Suprime-Cam survey and SDSS DR12 QSO database, Onoue et al. (2018) found that QSO pairs trace $>5\sigma$ overdense regions over 15 co-Mpc. These overdense regions could be protoclusters with $M_{z=0} > 10^{14}\ M_{\odot}$. ELAN0101+0201 is associated with one of the smallest-separation QSO pairs at $z \approx 2$. In the KCWI FoV ($\sim$100 physical kpc), we revealed another bright LAE with a broad Lyα emission. If this LAE is another AGN, then the AGN clustering in this field is even stronger than the AGN quartet system reported in Hennawi et al. (2015), implying a physical connection between this ELAN and a massive overdensity.

From Figure 3, over a larger FoV of $40'' \times 60''$, we detect another three bright LAE candidates from the PCWI data with $L_{\rm Ly\alpha} > 0.8L_{\rm Ly\alpha}^{*}$ (Table 1). In random fields, one expects $\approx$0.05 LAEs within this luminosity range and survey volume at $z \approx 2.2$ (e.g., Ciardullo et al. 2012) This further suggests that ELAN0201+0101 resides in the progenitor of a massive cluster.

As in Section 4.1, to interpret the discovery of the ELAN we assume that the optically thin, cool gas ($T \sim 10^4$ K) has an average column density of $N_{\rm H} \approx 10^{20.5}\,{\rm cm^{-2}}$ across the ELAN. The cool gas mass can be calculated using the $N_{\rm H} \times A_{\rm nebula} \times m_{\rm H}$, where $A_{\rm nebula}$ is the area of the nebula, and $m_{\rm H}$ is the atomic hydrogen mass. One can calculate that this ELAN could contain a reservoir of cool gas with the mass of $\approx 10^{11}\ M_{\odot}$ (see also Hennawi et al. 2015). The association between cool gas reservoirs and massive overdensities is unexpected. Cosmological simulations suggest that by $z \sim$ 2–3, baryons in the cluster progenitors ($M \gtrsim 10^{13}\ M_{\odot}$) are dominated by a hot, shock-heated gas with $T \sim 10^7$ K (Fumagalli et al. 2014; Faucher-Giguère et al. 2015). ELAN0101+0201 provides further challenges to these simulations. Recently, McCourt et al. (2018) and Ji et al. (2018) suggested that such inconsistencies may be solved if the cold gas takes the form of tiny fragments, sparsely distributed analogous to a mist.

4.3. The Profile of the Lyα Emission

With KCWI, we reveal high S/N Lyα emission and absorption throughout this system. From Figure 2, once can see that LAE1 has a highly asymmetric Lyα profile and contains a broad component (FWHM = $840\,{\rm km\,s^{-1}}$ and a narrow component (FWHM = $170\,{\rm km\,s^{-1}}$). The broad component is much wider than typical star-forming galaxies ($\approx$300–400 $\rm km\,s^{-1}$, e.g., Trainor et al. 2016), indicating that LAE1 could be an AGN, making this field likely hosting three AGNs on a $\sim$100 kpc scale. The narrow component could arise from the narrowline region or from the star formation of the host galaxy. The left wing of the broad component is strongly suppressed by the absorption.

Lyα is a resonant line and its profile may depend on the kinematics of the local ISM. An ISM outflow could cause the asymmetric Lyα emission (Dijkstra et al. 2006; Yang et al. 2014). An alternative source of asymmetry is enhanced by IGM absorption along the sightline that could suppress the blue peak, making the Lyα line asymmetric. From Section 4.2, ELAN0101+0201 resides in a massive overdensity. Such overdensities may be associated with a significant IGM H I overdensity. Cai et al. (2016, 2017) discussed how massive overdensities yield coherently strong Lyα absorption (CoSLAs) on $\approx$20 comoving Mpc scales. These CoSLAs consist of the superposition of a series of Lyα absorbers with $N_{\rm H\,I} = 10^{14-18}\,{\rm cm^{-2}}$ over $\approx$20 Mpc scales. This H I reservoir is likely to suppress the blue wing of the LAE1 and make the Lyα emission highly asymmetric.

In summary, we present ELAN0101 using this QSO pair selection method. It has an end-to-end size of 240 kpc and Lyα luminosity of 5×10^{44} erg s^{-1}. The Lyα size is smaller than that of the Jackpot, Slug, and MAMMOTH-1 nebulae. Note that the Slug and Jackpot nebulae are selected from a much larger sample of ≈20 ultraluminous QSOs, while ELAN0101 is the first target observed using the QSO pair method. The detection of such a large nebulosity provides a great opportunity to apply this selection technique to a larger sample. In the future, we will present our complete sample of 12 QSO pairs using PCWI and KCWI observations. Through deep IFS observations on this unique sample, we will conduct a statistical study of the Lyα spatial extent and gas kinematics, revealing how CGM gas fuels massive halos. With this survey, we will build a unique statistical sample to study the multiphase gas content in overdensities at $z \sim 2$ and provide important constraints to the formation and evolution of the hot, shock-heated ICM observed in the local universe.

Z.C. acknowledges the support provided by NASA through the Hubble Fellowship grant HST-HF2-51370 awarded by the Space Telescope Science Institute, which is operated by the Association of Universities for Research in Astronomy, Inc., for NASA, under contract NAS 5-26555. E.H. acknowledges the National Science Foundation under grant No. AST-1402206. S.C. gratefully acknowledges support from Swiss National Science Foundation grant PP00P2_163824.

Appendix

A.1. Absorption Pair Systems Detected in our KCWI Observations

In Figure 2, we discover a strong absorption pair, marked using the gray vertical lines. In Figure 4, we present that this pair has the best-fit column density of $N_{\rm H\,I} \approx 10^{15-18}$ cm^{-2}. For the Lyα forest with $N_{\rm H\,I} > 10^{15}$ cm^{-2}, previous studies suggest that such an absorption traces circumgalactic gas. Using the stacking of SDSS spectra, Pieri et al. (2014) argued that Lyα absorption column density of $N_{\rm H\,I} \sim 10^{15-17}$ cm^{-2} trace the CGM CIV absorption with column density of $N_{\rm C\,IV} \sim 10^{13.5\pm0.5}$ cm^{-2}. However, there have been no direct detections of galaxy-absorption within this column density range at $z = 2$–3. Although this is only one pair of the strong Lyα absorbers, our KCWI observations support that these strong Lyα clouds ($N_{\rm H\,I} = 10^{15-18}$ cm^{-2}) have a coherent length greater than 10 kpc, and such absorption system may trace a low Lyα-based SFR of $\lesssim$1.5 $M_\odot$ yr^{-1} within $R \lesssim 150$ projected kpc (see Section 3.4). In future, more systematic IFS studies on a statistical Lyα absorption sample at $z \approx 2$–3 will further constrain or reveal the nature of the galaxies associated with strong absorption systems. The SFRs and the impact parameters between galaxies and absorption can also directly constrain the models of galactic inflow and outflow (e.g., Oppenheimer et al. 2009; Cai et al. 2016).

Other than the strong absorption pair discussed above (see also Figures 2 and 4), two additional absorption features (~ -600 km s^{-1}) can be found in the spectra of both Q1 and Q2. We do not detect Lyα emitters in our KCWI data that are associated with both absorption pairs. Both absorption pairs are within the Lyα forest regime ($N_{\rm H\,I} < 10^{14}$ cm^{-2}). The discovery of these absorption pairs is consistent with several previous studies (e.g., Meiksin & Bouchet 1995; Coppolani et al. 2006) showing that the transverse correlation length of Lyα forest is on a large scale of a few to ten arcmin (see also Petitjean et al. 1998; Aracil et al. 2002). The non-detection of the Lyα emission associated with both systems is consistent with the expectation that the lower column-density Lyα forest may arise from the IGM filaments, rather than the circumgalactic gas.

ORCID iDs

Zheng Cai https://orcid.org/0000-0001-8467-6478
James D. Neill https://orcid.org/0000-0002-0466-1119

References

Alexander, D. M., Swinbank, A. M., Smail, I., McDermid, R., & Nesvadba, N. P. H. 2010, MNRAS, 402, 2211
Aracil, B., Petitjean, P., Smette, A., et al. 2002, A&A, 391, 1
Arrigoni Battaia, F., Hennawi, J. F., Cantalupo, S., & Prochaska, J. X. 2016, ApJ, 829, 3
Arrigoni Battaia, F., Hennawi, J. F., Prochaska, J. X., & Cantalupo, S. 2015a, ApJ, 809, 163
Arrigoni Battaia, F., Prochaska, J. X., Hennawi, J. F., et al. 2018, MNRAS, 473, 3907
Arrigoni Battaia, F., Yang, Y., Hennawi, J. F., et al. 2015b, ApJ, 804, 26
Borisova, E., Cantalupo, S., Lilly, S. J., et al. 2016, ApJ, 831, 39
Cai, Z., Fan, X., Peirani, S., et al. 2016, ApJ, 833, 135
Cai, Z., Fan, X., Yang, Y., et al. 2017, ApJ, 837, 71
Cantalupo, S. 2017, Gas Accretion onto Galaxies, 430, 195
Cantalupo, S., Arrigoni-Battaia, F., Prochaska, J. X., Hennawi, J. F., & Madau, P. 2014, Natur, 506, 63
Cantalupo, S., Lilly, S. J., & Haehnelt, M. G. 2012, MNRAS, 425, 1992
Cantalupo, S., Porciani, C., Lilly, S. J., & Miniati, F. 2005, ApJ, 628, 61
Ciardullo, R., Gronwall, C., Wolf, C., et al. 2012, ApJ, 744, 110
Coppolani, F., Petitjean, P., Stoehr, F., et al. 2006, MNRAS, 370, 1804
Dijkstra, M., Haiman, Z., & Spaans, M. 2006, ApJ, 649, 37
Faucher-Giguère, C.-A., Hopkins, P. F., Kereš, D., et al. 2015, MNRAS, 449, 987
Fumagalli, M., Hennawi, J. F., Prochaska, J. X., et al. 2014, ApJ, 780, 74
Harrison, C. M., Alexander, D. M., Mullaney, J. R., & Swinbank, A. M. 2014, MNRAS, 441, 3306
Hennawi, J. F., & Prochaska, J. X. 2013, ApJ, 766, 58
Hennawi, J. F., Prochaska, J. X., Cantalupo, S., & Arrigoni-Battaia, F. 2015, Sci, 348, 779
Ji, S., Peng Oh, S., & McCourt, M. 2018, MNRAS, 476, 852
Kennicutt, R. C., & Evans, N. J. 2012, ARA&A, 50, 531
Kollmeier, J. A., Zheng, Z., Davé, R., et al. 2010, ApJ, 708, 1048
Lau, M. W., Prochaska, J. X., & Hennawi, J. F. 2016, ApJS, 226, 25
Lusso, E., Worseck, G., Hennawi, J. F., et al. 2015, MNRAS, 449, 4204
Martin, D. C., Chang, D., Matuszewski, M., et al. 2014, ApJ, 786, 106
Martin, D. C., Matuszewski, M., Morrissey, P., et al. 2015, Natur, 524, 192
McCourt, M., Oh, S. P., O'Leary, R., & Madigan, A.-M. 2018, MNRAS, 473, 5407
Meiksin, A., & Bouchet, F. R. 1995, ApJL, 448, L85
Onoue, M., Kashikawa, N., Uchiyama, H., et al. 2018, PASJ, 70, S31
Oppenheimer, B. D., Davé, R., & Finlator, K. 2009, MNRAS, 396, 729
Pâris, I., Petitjean, P., Aubourg, E., et al. 2017, arXiv:1712.05029
Petitjean, P., Surdej, J., Smette, A., et al. 1998, A&A, 334, L45
Pieri, M. M., Mortonson, M. J., Frank, S., et al. 2014, MNRAS, 441, 1718
Prescott, M. K. M., Dey, A., & Jannuzi, B. T. 2009, ApJ, 702, 554
Shen, S., Madau, P., Guedes, J., et al. 2013, ApJ, 765, 89
Stewart, K. R., Kaufmann, T., Bullock, J. S., et al. 2011, ApJL, 735, L1
Trainor, R. F., Strom, A. L., Steidel, C. C., & Rudie, G. C. 2016, ApJ, 832, 171
Valentino, F., Daddi, E., Finoguenov, A., et al. 2016, ApJ, 829, 53
Villar-Martín, M., Sánchez, S. F., Humphrey, A., et al. 2007, MNRAS, 378, 416
White, M., Myers, A. D., Ross, N. P., et al. 2012, MNRAS, 424, 933
Yang, Y., Zabludoff, A., Jahnke, K., & Davé, R. 2014, ApJ, 793, 114